Journal of Power Sources 195 (2010) 4963–4970

Contents lists available at ScienceDirect

Journal of Power Sources

journal homepage: www.elsevier.com/locate/jpowsour

Study and development of non-aqueous silicon-air battery

Gil Cohn, Yair Ein-Eli*

Department of Materials Engineering, Technion-Israel Institute of Technology, Haifa 32000, Israel

ARTICLE INFO

Article history:
Received 29 December 2009
Received in revised form 22 February 2010
Accepted 22 February 2010
Available online 1 March 2010

Keywords:
Silicon-air
Battery
Ionic liquid
Mechanism
Limitations

ABSTRACT

Silicon-air battery utilizing a single-crystal heavily doped n-type silicon wafer anode and an air cathode is reported in this paper. The battery employs hydrophilic 1-ethyl-3-methylimidazolium oligofluorohydrogenate [EMI·$(HF)_{2.3}$F] room temperature ionic liquid electrolyte. Electrochemical studies, including polarization and galvanostatic experiments, performed on various silicon types reveal the predominance performance of heavily doped n-type. Cell discharging at constant current densities of 10, 50, 100 and 300 μA cm^{-2} in ambient atmosphere, shows working voltages of 1.1–0.8 V. The study shows that as discharge advances, the moist interface of the air electrode is covered by discharge products, which prevent a continuous diffusion of oxygen to the electrode–electrolyte interface. The oxygen suffocation, governed by the settlement of the cell reaction products, is the main factor for an early failure of the cells. Based on the results obtained from scanning electron microscopy, energy-dispersive X-ray spectroscopy and X-ray photoelectron spectroscopy studies, we propose a series of reactions governing the discharge process in silicon-air batteries, as well as a detailed mechanism for silicon oxide deposition on the air electrode porous carbon.

1. Introduction

Metal-air batteries have been attracting the electrochemistry research and development community for the last 50 years. Their attractiveness lies in the principle that the cathodic reaction is a catalyzed reduction of oxygen consumed from the environment, rather than stored in the system. This aspect results in high energy densities (W h l^{-1}) and high specific energies (W h kg^{-1}) for the metal-air batteries.

Most metal-air batteries, including Zn-air [1–3], Al-air [4,5] and Fe-air [6] utilize aqueous alkaline solutions, mainly potassium hydroxide (KOH), due to the high conductivity of such electrolyte and the superb ability to regulate the reduced oxygen ion into hydroxide anions [7]. Zn-air batteries has received broad attention in the 1960s and 1970s, with the development of commercialized primary cells, in coin type structure, for hearing aids operation, although in the last 10 years there has been an enormous effort to construct large scale Zn-air batteries for electric vehicles (EVs) [8]. The Al-air couple has higher theoretical densities compared to its competitors (Zn-air, Fe-air) and was under investigation as a suitable power source for vehicles and some stationary application [9]. However, high open circuit corrosion rates lead to the consumption of the Al metal anode without any usable power output. The lithium-air battery presents the highest theoretical specific energy value (11,246 W h kg^{-1}). However, Li suffers from severe corrosion in alkaline electrolytes [10] and safety concerns are still unresolved with aqueous systems. In 1996, Abraham and Jiang first reported [11] on a conducting polymer electrolyte based secondary lithium-air battery. This battery showed open circuit potential (OCP) of about 3 V and working voltage in the range of 2–2.8 V. Good coulombic efficiency was kept for only a few cycles. Ever since the lithium-air couple has been introduced it has been a subject for rapidly growing research.

In a recent communication, we have briefly discussed the construction of new, silicon based, metal-air battery [12]. From thermodynamic point of view, silicon exhibits attractive characterizations as an anode in metal-air batteries [12]. Unlike lithium, the world is ample with silicon (the second most plentiful element on earth crust) and it does not exhibit any safety issues. Silicon is non-toxic, and the reaction product with oxygen, SiO_2, can be handled and disposed without any special measurements.

Room temperature ionic liquids (RTILs) are a relatively new group of materials that are being introduced as batteries electrolytes. These electrolytes exhibit wide electrochemical window, high chemical and thermal stability, high ionic conductivity, low vapor pressure and low toxicity. Their non-flammability, high thermal stability and low heat of reaction make them desirable especially in lithium batteries [13,14]. The EMI (1-ethyl-3-methylimidazolium, Fig. 1a) cation based RTILs group show as well low viscosity, thus high conductivity. Hagiwara et al. [15] reported the synthesis of EMI·$(HF)_{2.3}$F RTIL (Fig. 1) by a reaction of EMICl and

* Corresponding author. Tel.: +972 4 829 4588; fax: +972 4 829 5677.
E-mail address: eineli@tx.technion.ac.il (Y. Ein-Eli).

0378-7753/$ – see front matter © 2010 Elsevier B.V. All rights reserved.
doi:10.1016/j.jpowsour.2010.02.070

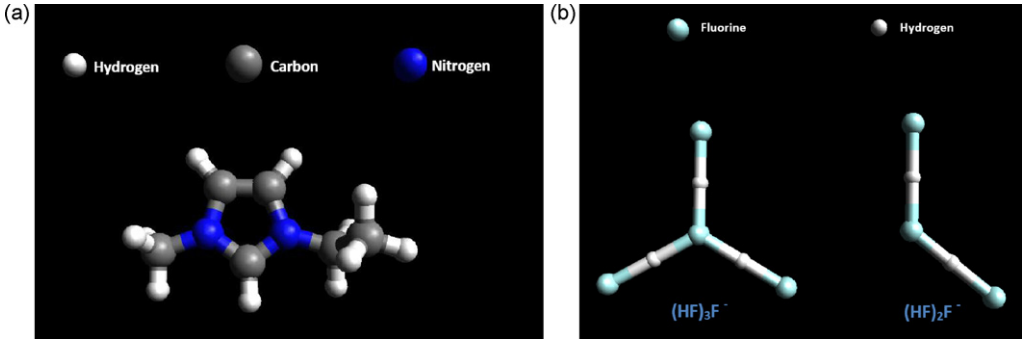

Fig. 1. Schematic diagram of the EMI·$(HF)_{2.3}F$ RTIL electrolyte chemical structure: (a) EMI cation, (b) H_3F_4 (30%) and H_2F_3 (70%) anions.

hydrogen fluoride. This RTIL possesses some interesting properties, such as high conductivity (100 mS cm^{-1}, the highest among RTILs of its kind), low viscosity and chemical stability in air. Furthermore, Raz et al. reported [16,30] on the anodic dissolution reaction of EMI·$(HF)_{2.3}F$ RTIL with n-type silicon and the formation of macroporous over the silicon surface, without illumination.

In the present work, we describe the study and development of a silicon-air battery with the unique structure of [Si wafer|EMI·$(HF)_{2.3}F$|air]. Detailed cell discharge mechanism and in-depth study of Si-air battery electrochemical behavior and characteristics are described, as well.

2. Experimental

2.1. Materials

Silicon single-crystal wafer anode electrodes were varied in their doping level, dopant type and orientation. Heavily doped n-type wafers, including ⟨1 0 0⟩ As-doped (0.001–0.005 Ω cm), ⟨1 1 1⟩ As-doped (0.001–0.007 Ω cm), ⟨1 1 1⟩ Sb-doped (<0.02 Ω cm) and ⟨1 0 0⟩ medium As-doped (0.1–0.6 Ω cm) were supplied by University Wafer (USA). Heavily doped p-type wafers, including ⟨1 0 0⟩ (0.001–0.005 Ω cm), ⟨1 1 1⟩ (0.005–0.01 Ω cm) and medium doped ⟨1 0 0⟩ (1–3 Ω cm) were supplied by Si-Mat (Germany). For cathode purpose, commercial air electrode (designed and formulated for alkaline Zn-air) was used, as supplied by Electric Fuel Inc. This air electrode comprised a polytetrafluoroethylene (PTFE) powder and carbon black (0.45–0.5 g cm^{-2} loaded) structure catalyzed by manganese dioxide pressed onto a nickel 200 mesh. Teflon microporous layer was attached to the air side of the electrode. RTIL EMI·$(HF)_{2.3}F$ served as the electrolyte. The IL was provided by R. Hagiwara from Kyoto University, Japan, and was synthesized according to methods described elsewhere [15].

2.2. Three electrodes cell preparation

Three electrodes cell configuration was used, with a single-crystal silicon wafer or air electrode serving as the working electrode, and platinum wires serving both as counter and quasi-reference electrodes. Experiments were carried out in an electrochemical cell containing a polypropylene holder of the silicon specimen, supported with a screwed back contact stainless steel plate. The exposed surface was 0.6 cm^2 (Fig. 2). Previous to any experiment the silicon sample was immersed in HF solution (1HF:5H_2O) for ten seconds in order to remove surface native oxide layer. The silicon was then rinsed with de-ionized (DI) water and dried using a nitrogen stream. After the cell was assembled, 0.5 ml of the ionic liquid was added.

2.3. Battery cell preparation

For silicon-air systems studies, a silicon single-crystal, air electrode (important note: as mentioned above, the air cathode was formulated to alkaline Zn-air) and ionic liquid were used. Schematic view of cell assembly is shown in Fig. 3. The cell was comprised of three plastic plates. Silicon wafers were cut to 1 cm × 1 cm pieces and were pressed into a viton O-ring, achieving 0.5 cm^2 exposed surface area. Air electrodes were cut into circular sheets, with 0.5 cm^2 exposed area, and outer circle periphery for electrical contact. Terminal contacts were established with Cu wires. Si wafer anodes were pretreated before cell construction as described in Section 2.2. Cells were held at OCP (open circuit potential) for duration of 4 h prior to initiation of the discharge process. This was performed in order to allow a proper wetting of the porous carbon (at the air cathode) with the RTIL electrolyte.

2.4. Electrochemical measurements and characterization

Silicon cyclic voltammetry, potentiodynamic and linear polarization studies were performed with EG&G Princeton Applied Research potentiostat/galvanostat 2273. Discharge experiments were carried out using Arbin BT2000 battery test equipment (Arbin Inc.). All experiments were conducted under ambient conditions. Surface morphologies of silicon electrode were studied using high resolution scanning electron microscope (HRSEM, Hitachi S 4700). SEM (FEI Quanta 200), equipped with energy-dispersive X-ray spectroscopy system (EDX, Oxford Inst.) was utilized in surface morphology studies and chemical analysis of the air electrodes. XPS analysis was performed using a Thermo VG Scientific, Sigma probe, X-ray photoelectron spectrometer with a base pressure in the 10^{-9} Torr, fitted with a monochromotized Al Kα (1486.6 eV) X-ray source.

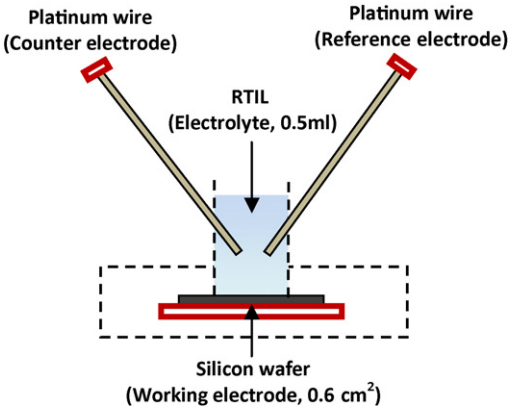

Fig. 2. Schematic diagram of the three electrodes electrochemical configuration.

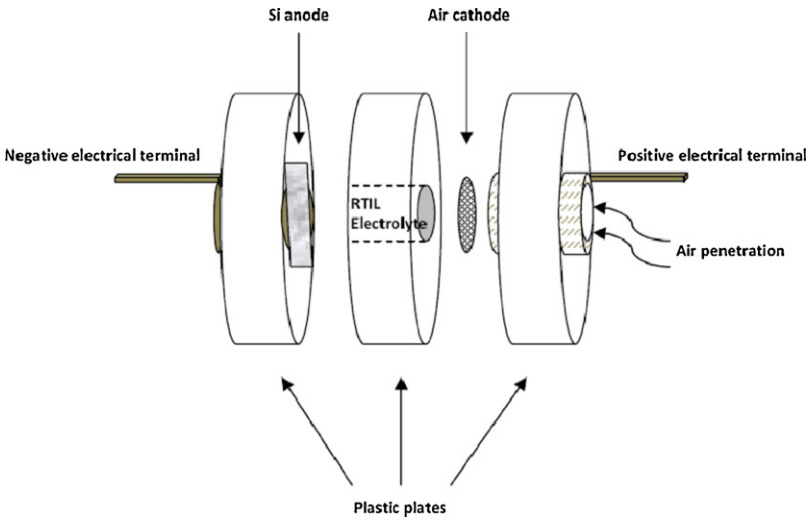

Fig. 3. Schematic diagram of the silicon-air battery cell and its components.

3. Results and discussion

3.1. Half-cell analysis

Our efforts regarding the development of Si-air battery were actually initiated with a much simpler, intuitive electrolyte, namely KOH. However, silicon undergoes an extreme fast corrosion process in alkaline solutions [17,18]. Silicon etching rate is measured to be in the order of tens of $\mu m\,min^{-1}$ and therefore, high rates of self-discharge processes are expected. EMI·$(HF)_{2.3}$F RTIL was chosen as an alternative electrolyte due to its special features, as described in the introduction section and due to the anodic features of Si revealed in previous study [16]. Table 1 presents Si corrosion currents and corrosion rates recorded for different wafers types, utilizing EMI·$(HF)_{2.3}$F RTIL electrolyte. The corrosion rates were calculated using the corrosion currents, obtained with the use of linear polarization experiments in the range of ±20 mV relative to OCP. The result shows high stability and negligible corrosion rates for silicon in EMI·$(HF)_{2.3}$F. It should be stated that silicon corrosion rates resemble corrosion rates of highly resistive metals in extreme environments, e.g. titanium in strong reducing agents [19].

In order to determine whether the coupling between EMI·$(HF)_{2.3}$F RTIL electrolyte, silicon anode and oxygen cathode can lead to reasonable battery performances, potentiodynamic experiments were conducted. Cathodic polarization of the air electrode and anodic polarizations profiles of several silicon wafers are shown in Fig. 4. It should be noted that the potentials difference at OCP conditions between the two half cells is 1.25–1.5 V, depending on the silicon type (Fig. 4). As can be seen in Fig. 4, there is no major difference in the anodic behavior of the various heavily doped n-type silicon (n^{++}) electrodes, i.e. no effect of dopant type and orientation. All heavily doped n-silicon electrodes showed no anodic passivity up to 1.3 V (vs. Pt) during the anodic polarization. On the other hand, the medium doped n-type curve (cyan curve, ◊ symbol in Fig. 4) (For interpretation of the references to color in this sentence, the reader is referred to the web version of the article.) does exhibit a passivation region along the whole anodic potential range. OCP values for the p-type silicon are 0.25–0.3 V more positive (anodic) than the corresponding n-type. This is in agreement with overall more negative OCP value for n-type than for p-type silicon [20].

The results shown in Fig. 4 and Table 1 present the difficulty in deciding which Si type should be further studied. In the low current density region (<1 mA cm^{-2}), n^{++} Si exhibits a wider potential window than the p^{++} silicon, with regard to the air electrode potential. However, once higher current densities are being considered of above 1 mA cm^{-2}, the resulting potential difference for p^{++} Si is the higher one; 1.05 V compared to 0.9 V for n^{++} silicon. Considering the self-corrosion rates, the choice becomes much complex: p^{++} silicon exhibits lower corrosion rates than n^{++}, hence longer shelf life. The decision was to continue the study primarily with n^{++} silicon, as the potential that the system can produce is the key issue in optimizing cell performance.

Table 1
Silicon electrodes corrosion currents (rates) in EMI·$(HF)_{2.3}$F.

Silicon type	Corrosion current ($\mu A/cm^2$)	Corrosion rate (nm/min)
n 1 0 0 (As)	8.71	0.16
n^{++} 1 0 0 (As)	4.23	0.08
n^{++} 1 1 1 (As)	4.22	0.08
n^{++} 1 1 1 (Sb)	3.71	0.07
p 1 0 0	1.29	0.02
p^{++} 1 0 0	0.54	0.01
p^{++} 1 1 1	0.42	<0.01

++ is designated for heavily doped silicon wafers.

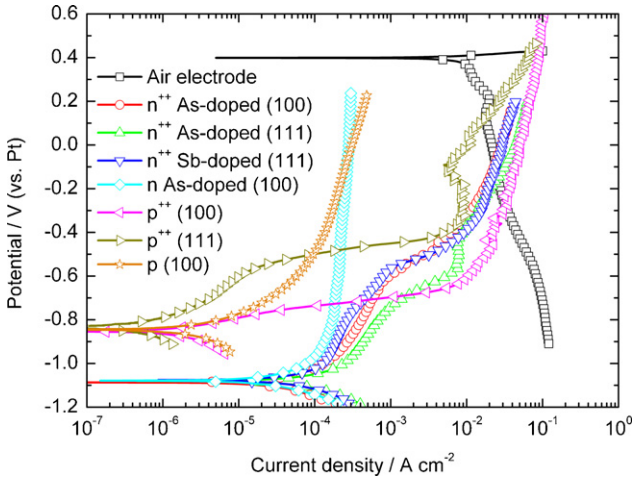

Fig. 4. Polarization voltammograms recorded with EMI·$(HF)_{2.3}$F RTIL at 5 mV s^{-1} for various electrodes: silicon single-crystal anodes and air cathodes.

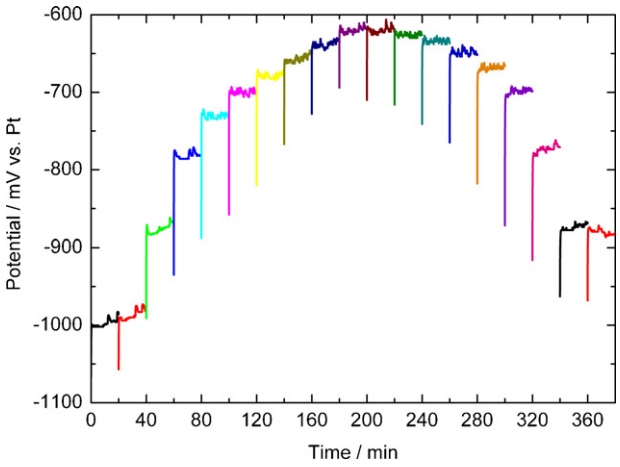

Fig. 5. Galvanostatic polarization of ⟨1 0 0⟩ heavily As-doped n-type silicon in EMI·$(HF)_{2.3}F$ (red curve, ◯ symbol in Fig. 4). Polarization conducted with current density of 100–1000 μA cm^{-2} and back to 100 μA cm^{-2}, in 100 μA cm^{-2} intervals, each for 20 min.

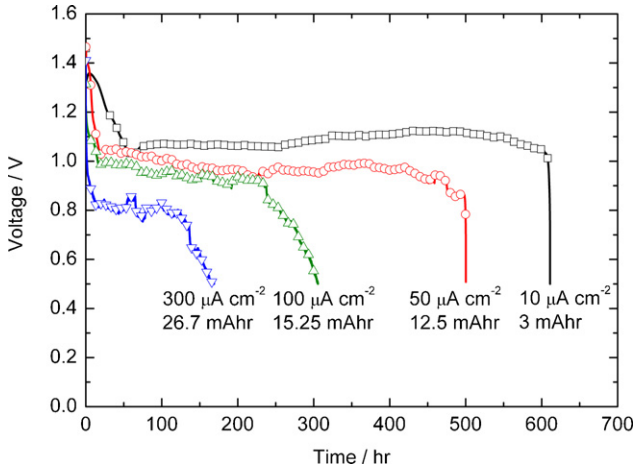

Fig. 6. Discharge plots of silicon-air cells using EMI·$(HF)_{2.3}F$ RTIL electrolyte at different constant current densities.

3.2. Galvanostatic discharge behavior

Fig. 5 shows galvanostatic polarization curve for n^{++} silicon electrode. The electrode was polarized against Pt counter electrode at different current densities, starting from 0.1 mA cm^{-2} up to 1 mA cm^{-2} and back to 0.1 mA cm^{-2}, with 0.1 mA cm^{-2} step for 20 min, resulting in up and down staircase curve. As expected, the obtained half-cell potential value is more positive as the current density increases. However, frequent fluctuations are observed in each step of the 20 min constant current polarization. The frequency of these fluctuations depends on the current density; as the current density increases the fluctuations detected in the specific measured potential appear in higher frequency. The fluctuations are attributed to the electrochemical formation of gaseous SiF_4, (as was already reported in Ref. [22]) as a product of the anodic reaction between EMI·$(HF)_{2.3}F$ RTIL and silicon. Each alteration in the potential-time profiles during a specific constant current step indicates a build-up and release of SiF_4 at the silicon surface. Thus, the anodic electrochemical dissolution of highly doped silicon EMI·$(HF)_{2.3}F$ RTIL is preformed according to the following suggested reaction sequence:

$$Si + 12(HF)_2F^- \rightarrow SiF_4 + 8(HF)_3F^- + 4e^- \quad (1)$$

Thus, anodic dissolution of silicon involves the formation of SiF_4, while 12 dihydrogen-fluoride anions of the IL transformed to 8 trihydrogenated-fluoride anions, also constitute the IL. It should be noticed that pristine IL is composed of a mixture of di-and trihydrogenated fluoride anions in a ratio of 7:3.

3.3. Silicon-air cell discharge performance

Silicon-air battery discharge performances under several current densities in ambient temperature, are shown in Fig. 6. The discharges were carried out in the cell configuration presented in Fig. 3. Data was collected using n^{++} As-doped silicon anode (red curve, ◯ symbol in Fig. 4). Prior to any discharge, the cell was held at OCP for 4 h, allowing the electrolyte to properly wet the porous carbon constitutes the air electrode. Discharge was terminated in a cut-off voltage of 0.5 V. As expected, the cell voltage decreases with increasing current density, due to polarization losses. The discharge potential is quite stable and relatively extended, with potential plateaus of 0.8–1.1 V, depending on the current density loads. The capacity values obtained for the Si-air battery discharges presented in Fig. 6 are 6, 25, 30.5 and 53.4 mAh cm^{-2} at current densities of 10, 50, 100 and 300 μA cm^{-2}, respectively (shown in Fig. 6 in cell capacity of 3, 12.5, 15.25 and 26.7 mAh). It could be expected that the discharge time (and hence the capacity) obtained at a current density of 10 μA cm^{-2} would be as high as 10 times than the time (capacity) recorded for silicon-air battery discharged at a current density of 100 μA cm^{-2}. However, the results presented here show that this is not the case. It can be deduced from the above numbers that there is no correlation between the discharge current and dis-

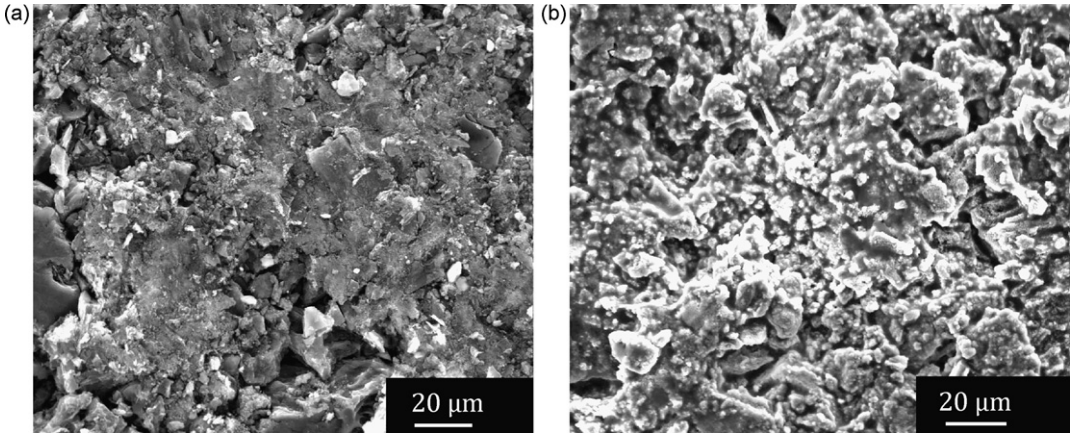

Fig. 7. SEM images of the air electrode surface (a) before and (b) after discharge at 0.1 mA cm^{-2} for 260 h.

charge time (capacity), i.e. the discharge process is not controlled by the anodic silicon dissolution only. It is interesting to note that the battery is more efficient once it is being discharged at high rates (100 and 300 μA cm^{-2}), compared with low battery efficiency at the slower rates (10 and 50 μA cm^{-2}). A suggested explanation for this unique behavior will be given in the next section.

In-course of SiF_4 formation at the silicon–electrolyte interface (Eq. (1)), we can suggest a complete description of the cell discharge reactions at the cathode side, by the following set of reactions:

$$O_2 + 12(HF)_3F^- + 4e^- \rightarrow 2H_2O + 16(HF)_2F^- \quad (2)$$

$$SiF_4 + 2H_2O + 4(HF)_2F^- \rightarrow SiO_2 + 4(HF)_3F^- \quad (3)$$

Oxygen is being reduced in the presence of 12 tri-hydrogenated fluoride anions to produce water and 16 di-hydrogenated fluoride anions and 2 water molecules, which further reacts with the SiF_4 produced during the anodic reaction to yield Si-dioxide and 4 tri-hydrogenated fluoride anions.

As was investigated before [21], the anion is the main charge carrier in the $EMI(HF)_{2.3}F$ RTIL. Therefore, no cation is written in the above reactions. The overall expected cell reaction, based on the two half-cell reactions discussed above, is therefore:

$$Si + O_2 \rightarrow SiO_2 \quad (4)$$

It should be noted that despite the general custom to present the capacity of a battery with units of mAh g^{-1}, in this case we prefer to present the discharge time as a capacity comparable. As in the case of Li-air batteries, non-soluble reaction products are deposited at the porous air electrode [23,24]. Therefore the level of carbon's porosity in the air electrode and the size of the exposed interface surface area have a significant influence on the cell capacity. Since no investigation has been done yet on the exact relationship between those two parameters and the capacity in such Si-air cells, we present actual discharging length rather than capacity or pseudo-capacity.

3.4. Discharge products

3.4.1. Air cathode side

3.4.1.1. Morphological studies. Since the battery utilizes silicon wafers, we expected the battery system to run as long as there was available silicon for the anodic reaction. However, that was not the case; After the sudden drop in the potential (see for example, current densities of 10 and 50 μA cm^{-2}, Fig. 6) and completion of the discharge to a cut-off potential of 0.5 V it was revealed that the silicon wafer was almost intact; At the most, only ~10% of the total theoretical silicon capacity was utilized. Such behavior, where the limiting factor is not the anodic fuel, may serve as a clear indication for a severe performance limitation at the air cathode. Such phenomenon was already observed in Li-air batteries [23,24], where the reaction products (Li_2O and Li_2O_2) are insoluble in the non-aqueous electrolyte. As a consequence, the reaction products are deposited at the porous carbon, preventing further reduction of O_2 molecules, leading to discharge termination. We suggest the same mechanism for the silicon-air battery; the reaction product, SiO_2, accumulates at the surface of the carbon air electrode, decreasing the available area for the reduction of oxygen and reducing the cell voltage. At the final steps of the discharge process, the air electrode is completely clogged, leading to suffocation and finally to pre-matured termination of the battery life. SEM micrographs, shown in Fig. 7a and b, support the above mechanism. The micrographs present the surface of the air electrode being exposed to the electrolyte, before discharge (Fig. 7a) and subsequent to discharge process of 260 h at a constant current of 0.1 mA cm^{-2} (Fig. 7b). It is evident from Fig. 7b that during discharge the air electrode is being covered with a residue layer.

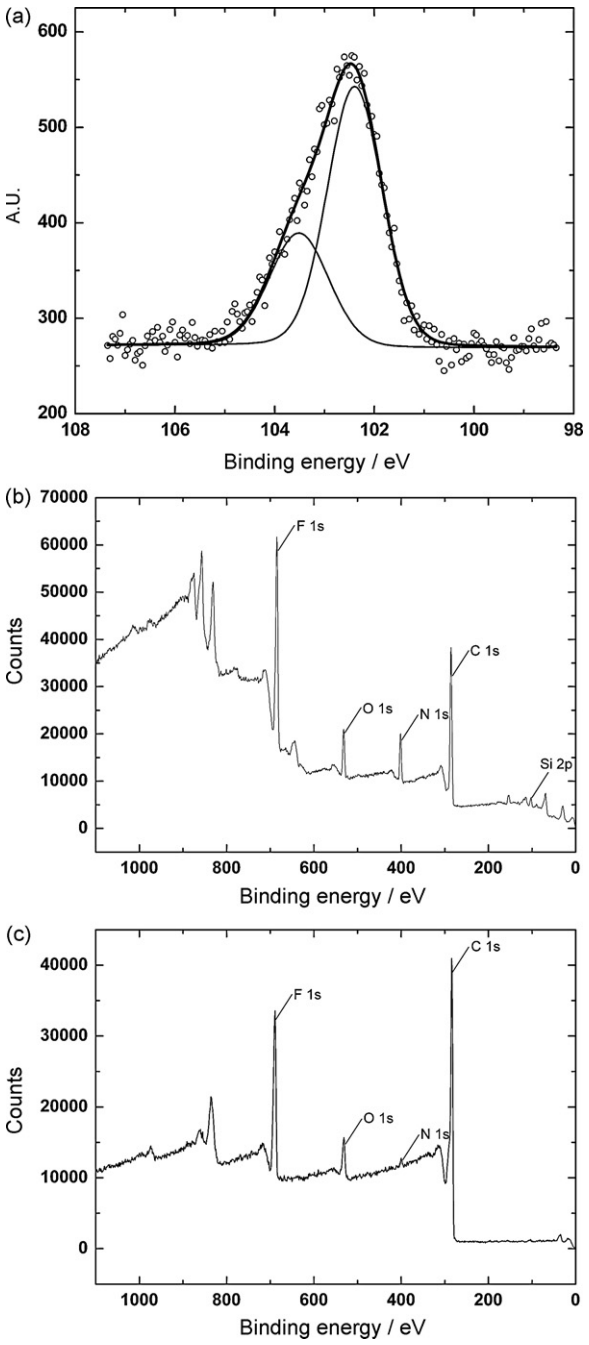

Fig. 8. XPS spectra obtained from the "wet" side of an air electrode: (a) Curve fitting of the Si 2p XPS spectrum after discharge at 0.1 mA cm^{-2} for 260 h; (b) Wide scan XPS spectrum after discharge at 0.1 mA cm^{-2} for 260 h; (c) Wide scan XPS spectrum of clean air electrode.

3.4.1.2. Surface chemistry at the air cathode. Energy-dispersive X-ray spectroscopy (EDX) analysis performed on the previously discussed air electrode sample showed the presence of Si over the air electrode surface. Silicon traces were assumed to be, according to Eq. (4), in the form of the reaction product SiO_2. In order to confirm the presence of silicon oxide at the air electrode, chemical bonding at terminal silicon was identified by the use of X-ray photoelectron spectroscopy (XPS). Fig. 8 shows the XPS spectra of an air electrode after discharge in a constant current of 0.1 mA cm^{-2} for 260 h, having n^{++} silicon as the anode. The Si 2p spectrum signal (Fig. 8a) can be de-convoluted into two separate peaks at 103.5 and 102.4 eV. The high binding energy peak corresponds to reported

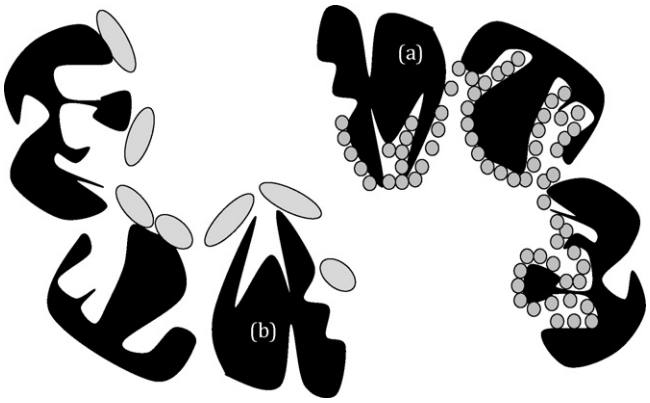

Fig. 9. A model for SiO_2 reaction product deposition on porous carbon air electrode. (a) Low discharge currents and (b) high discharge currents.

values of Si in the bonding of SiO_2 [25,26]. The low binding energy peak can be attributed to SiO_x ($0 < x < 2$), with a chemical shift of the SiO_2 peak towards lower binding energies. However, the ratio between the two peaks areas, with the SiO_x peak area twice as the SiO_2, may suggest other contribution to the 102.4 eV peak rather than SiO_2. A possible explanation may be due to the RTIL used, containing F^- ions. The low vapor pressure of the RTIL makes the drying of the air electrode highly difficult after it has been wetted. Therefore, residues of RTIL can still be present in the porous air electrode even after the drying process (90 °C in vacuum for 24 h). The presence of electronegative F^- ions in the air electrode results in the formation of Si–F or Si–O–F bonds, which shifts the XPS signal towards lower binding energies. Wide XPS scan recorded for the same sample is shown in Fig. 8b. The lines of F 1s and O 1s signals can be clearly identified in the spectrum. In addition to the presence of residues of the RTIL in the porous carbon, which contributes to the large magnitude of F 1s peak, F ions are also present in the PTFE binder mixed (with the active carbon). These F ions enhance the F 1s signal intensity. The effect of discharge process on the amount of oxygen at the air electrode can be understood once comparing the wide scan spectrum obtained subsequent to a discharge process (Fig. 8b) with a scan obtained from a pristine air electrode (Fig. 8c). In both spectra the O 1s peak is present, however the relative amount of oxygen is increased: 3.65 at.% in the pristine electrode, while subsequent to a discharge process the atomic percentage is almost doubled 6.37 at.%. Moreover, the Si 2p peak presented in Fig. 8b (enlarged in Fig. 8a) is missing from the spectrum taken from a fresh air electrode (Fig. 8c). Therefore, it can be concluded that the reaction product is indeed SiO_2, which is being deposited during discharge on the moist surface of the air electrode, eventually leading to a termination of further battery operating.

As was discussed earlier and can also be seen in Fig. 6, the discharge capacity is strongly related to the discharge current density. As mentioned before, no opposite correlation is observed between the discharge current and discharge capacity. Usually, one would expect from a battery a higher discharge capacity at a lower current density. The opposite results shown here, along with SiO_2 deposits at the air cathode (shown in Fig. 7b), can be explained in the following manner: activated carbon in the air electrode consists of different pore sizes, from micro (0.7–2 nm)-, to meso (2–50 nm)- and macro (>50 nm)-pores (Fig. 9) [27]. These pores structures, and the relative amount of the different pores sizes, determines the surface area of the air electrode. The surface area is comprised of both the surface area of the micro-pores and of the meso- and macro-pores. However, the actual surface area is determined mostly by the micro-pores surface. These surface areas are the available sites for oxygen reduction reaction, necessary for the cell operation. Therefore, it would be expected that electrodes with high surface areas would result in cells having an increased capacity. However, as was already shown before, this assumption is not valid [24,28,29]. The critical factor, determines the cell capacity is the distribution and percentage of the different sized pores. During discharge, the pores are being filled with deposits of the reaction products. The size and volume of the deposited particles is mostly affected by the discharge current density. Discharge process performed at high current densities would lead to the formation of coarse and bulky deposits, while discharge process at lower current densities would produce finer solid deposits. As a consequence of this divergence in the size of the oxides, the sites where the deposition takes place are diversed as well. The finer particles, formed at low current densities, are deposited at the micro-pores surface sites, as described in Fig. 9a. With the advance in the discharge process, the micro-pores are filled with the small particles, decreasing the path for oxygen diffusion and reduction. Those areas are no longer active and thus do not contribute to the cell operation. Therefore, low capacity values (even though long discharge times) are obtained at low current densities discharge, as shown in Fig. 6. The accumulation of small oxide particles at the surface of the micro-pores blocks the path for oxygen diffusion, with only a relative small amount of consumed silicon anode, i.e. low capacity.

On the other hand, when high current densities are applied the micro-pores are not being filled with discharge reaction products. Since the deposited particles are much coarser and thus not being deposited and accumulated at the micro-pores, oxygen diffusion is still available through the micro-pores, while the deposition takes place at the meso- and macro-pores sites. This process now enables increased capacities while discharging the cell at relatively high current densities. The discharge continues with high rate, achieving higher capacities, until the entire surface is blocked for good, with a continuous silicon oxide layer, as describes in Fig. 9b. An image of the amount and distribution of the silicon oxide particles on the air electrode, subsequent to different discharge profiles, was obtained with the use of back-scattered electrons (BSE) micrographs and EDX element distribution map (K-line) of silicon at the air electrode. Fig. 10 presents the silicon distribution after discharging in current densities of 100 $\mu A\,cm^{-2}$ (Fig. 10a and b) and 300 $\mu A\,cm^{-2}$ (Fig. 10c and d). It can be easily observe that with increasing current densities, the amount of silicon dispersed on the air electrode is increased (brighter dotes) and more surface area is being covered. With the highest current density of 300 $\mu A\,cm^{-2}$, the surface is almost completely covered with coarse oxide particles covering the air electrode carbon surface. On the other hand, discharge at low current density of 100 $\mu A\,cm^{-2}$ provides a fine coverage of the air cathode. The mapping shows that the amount of the oxide is significantly higher once discharge is being performed at higher current density. Thus the cartoon presented in Fig. 9 reflects well the unique situation of silicon-air batteries utilizing non-aqueous electrolytes, where the reaction zone occurs at the electrolyte-air cathode interface. Overall, this layer prevents any further reaction involving oxygen from the backside of the air electrode and electrolyte in the front.

3.4.2. Silicon anode side

Fig. 11 presents HRSEM images obtained from silicon anodes (100 n^{++} As-doped) subsequent to a partial discharge of Si-air cells at different current densities and different discharge lengths. Micrograph 11a shows silicon anode surface after short discharge (135 h) at low current density of 10 $\mu A\,cm^{-2}$. It can be seen that the dissolution of silicon proceeds initially inconsistently, forming pits, as well as preserving the pristine wafer surface integrity at some locations. Increasing the current density 20 times to 200 $\mu A\,cm^{-2}$, while preserving the discharge time (micrograph 11b), resulted in increased termination of the smooth silicon surface, and the formation of 1 μm diameter shallow craters. However, lowering the

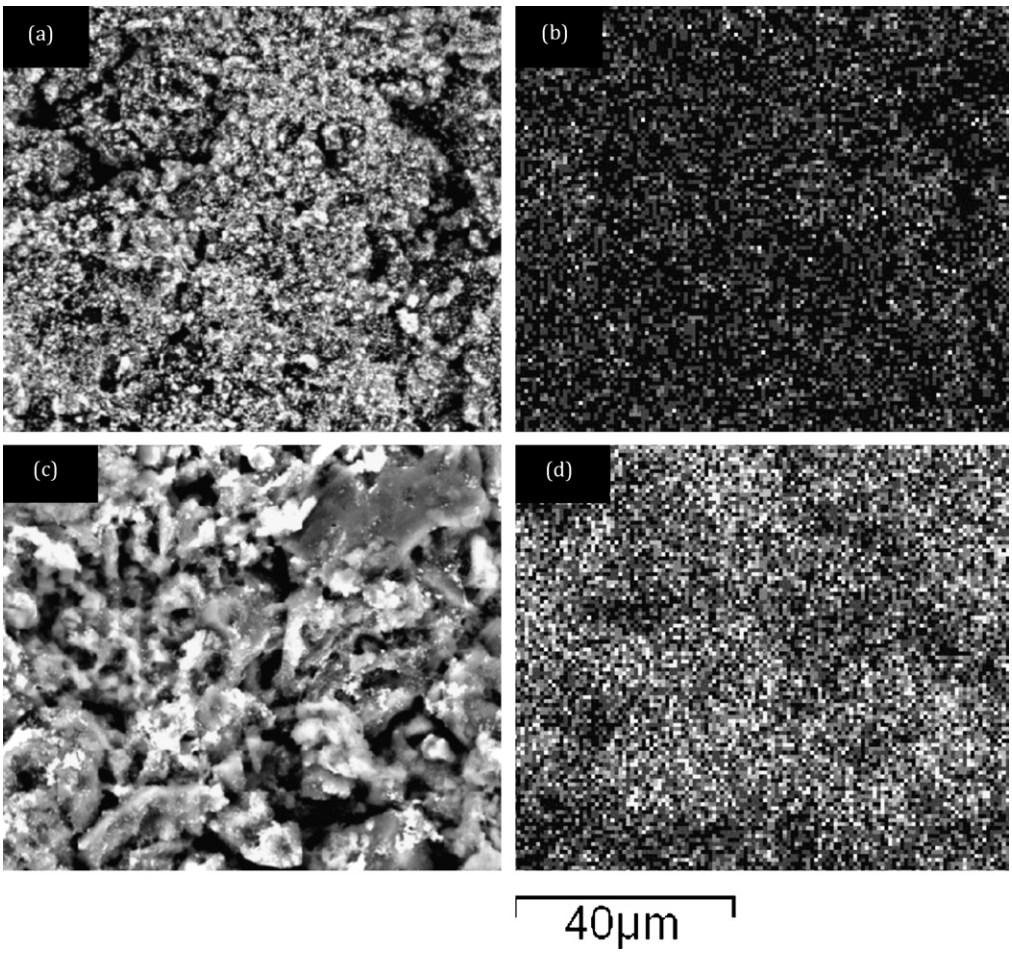

Fig. 10. BSE micrographs and EDX element distribution maps (K-line) of silicon on the air electrode taken after discharge at (a and b) 100 μA cm^{-2} for 300 h, and (c and d) 300 μA cm^{-2} for 150 h.

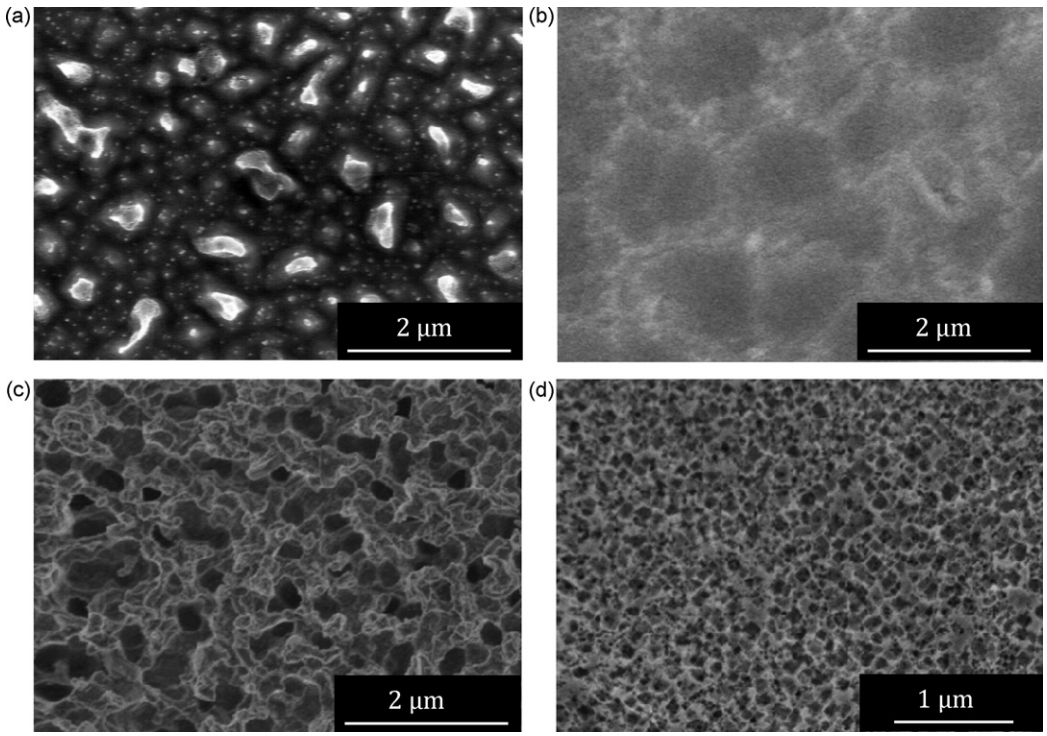

Fig. 11. HRSEM micrographs of silicon surface evolution during battery operation: (a) 135 h at a current density of 10 μA cm^{-2}, (b) 140 h at a current density of 200 μA cm^{-2}, (c) 450 h at a current density of 100 μA cm^{-2}, and (d) 114 h at a current density of 400 μA cm^{-2}.

current density to 100 $\mu A\,cm^{-2}$ yields an expansion of the discharge to 450 h and the producing of a deep porous silicon structure, with pore size distribution of 300–600 nm (Fig. 11c). Micrograph 11d shows silicon surface after discharge at the same capacity as micrograph 11c, however with a discharge current density of 400 $\mu A\,cm^{-2}$ for 114 h. This discharge resulted in the formation of finer pores (100 nm) with much denser distribution, relative to the structure shown in micrograph 11c. Such porous silicon structure formation during battery discharge operation can further support high current loads, as more active silicon anode surface area is progressively exposed upon cell discharging.

3.4.3. Silicon anode surface chemistry

Recently, Raz et al. have published a detailed study on the surface films formed on silicon upon anodic polarization [30]. It was established that the formation of porous silicon (PS) is possible due to successive cycles of Si–F bond formation at the silicon surface and silicon etching. Competitive etching and pore formation are responsible for both the dissolution and the formation of the obtained porous structure. Dissolution/etching during anodic polarization proceeds due to a branching process along the pores, which causes the upper pore structure to peel-off, exposing the bottom's pore surface. As the discharge time or increase in current density or both of these two occurs, wider and deeper porous structures are formed, as well as deeper etching, leading to increased silicon discharge. The formation and existence of Si–F compounds were reported previously in earlier studies, studying the formation of PS from p-Si under anodic polarization in EMI$(HF)_{2.3}$F solution using *in situ* FTIR and XPS [16,22,30]. Therefore, it is reasonable to assume that the anodic dissolution of n-type silicon anode in the battery is accompanied by the formation of SiF_4. The high dissolution ability of silicon in the specific IL is attributed to the ability of the room temperature molten salts to form Si–F bonds in course of anodic polarization taking place during battery discharge. It is postulated that Si dissolution can occur due to unique conditions existing in this electrolyte, providing a high concentration of fluoride anions under battery discharge operation.

4. Conclusions

This paper describes the efforts in studying and developing rather unique non-aqueous primary silicon-air battery. This system is comprised of single-crystal silicon wafers as the anode and EMI·$(HF)_{2.3}$F room temperature ionic liquid as the electrolyte. Prime objective of the research was to identify the most appropriate silicon type to serve as the anodic active material. From the suggested types of silicon wafers, heavily doped n-type was found to be the most potent, as it combines negligible self-corrosion rate together with cell potential varies from 1.1 to 0.8 V, with current densities of 10–300 $\mu A\,cm^{-2}$, accordingly. The anodic dissolution of silicon and the formation of SiO_2 as the reaction product are being described in multi steps reaction process. The formation of SiF_4 during discharge is accompanied with periodic brief decrease in the silicon potential, a phenomena that can be observed in half-cell galvanostatic experiments. EDX and XPS examination confirm the sedimentation of SiO_2 over the air electrode. This deposit is considered to cause pore clogging in the active carbon layer of the air electrode and decrease of available active sites for oxygen reduction. These results show that the battery capacity is limited by the air electrode rather than anodic material. Thus, it is highly important to study and develop a robust air cathode capable of extending the battery life.

Further studies will enhance the practical specific energy and power densities of the new silicon-air battery, as materials and engineering optimization are required. Continuous study should examine improvements in silicon type selections, developing a suitable air cathode, while electrolyte modification should be bear in mind. However, the enormous range of applications for this new air battery, starting from MEMS (Micro-Electro-Mechanical Systems) and up to mechanically rechargeable batteries for EVs, will contribute to a growing interest in this technology.

Acknowledgements

The work was primarily supported by the Carl E. Schustak R&D Energy Fund of the Technion Research Foundation and by the United States – Israel Binational Science Foundation (BSF). The authors express thanks to Professor Rika Hagiwara from the Department of Fundamental Energy Science in Kyoto University, Japan, for supplying EMI·$(HF)_{2.3}$F RTIL.

References

[1] C. Chakkaravarthy, A.K.A. Waheed, H.V.K. Udupa, J. Power Sources 6 (1981) 203.
[2] K.F. Blurton, A.F. Sammells, J. Power Sources 4 (1979) 263.
[3] C. Chakkaravarthy, H.V.K. Udupa, J. Power Sources 10 (1983) 197.
[4] T. Våland, O. Mollestad, G. Nilsson, Al-air cells—potential small electric generators for field use, in: J. Thompson (Ed.), Power Sources, vol. 8, International Power Sources Symposium, Leatherhead, UK, 1993, pp. 523–534.
[5] Y. Hori, J. Takao, H. Shomon, Electrochim. Acta 30 (1985) 1121.
[6] L. Öjefors, L. Carlsson, J. Power Sources 2 (1977) 287.
[7] D.A. Lown, H.R. Thirsk, Trans. Faraday Soc. 67 (1971) 132.
[8] J. Goldstein, B. Koretz, IEEE Aerospace Electron. Syst. Mag. 8 (1993) 36.
[9] J.F. Cooper, E.L. Littauer, Mechanically Rechargeable, Metal-air Batteries for Automotive Propulsion, UCRL-81178, May 26, 1978.
[10] E.L. Littauer, K.C. Tsai, J. Electrochem. Soc. 124 (1977) 850.
[11] K.M. Abraham, Z. Jiang, J. Electrochem. Soc. 143 (1996) 1.
[12] G. Cohn, D. Starosvetsky, R. Hagiwara, D.D. Macdonald, Y. Ein-Eli, Electrochem. Commun. 11 (2009) 1916.
[13] H. Ye, J.J. Xu, ESC Trans. 3 (2008) 73.
[14] H. Sakaebe, H. Matsumoto, K. Tatsumi, Electrochim. Acta 53 (2007) 1048.
[15] R. Hagiwara, T. Hirashige, T. Tsuda, Y. Ito, J. Electrochem. Soc. 149 (2002) D1.
[16] O. Raz, D. Starosvetsky, T. Tsuda, B.T. Nohira, R. Hagiwara, Y. Ein-Eli, Electrochem. Solid-State Lett. 10 (2007) D25.
[17] H. Seidel, L. Csepregi, A. Heuberger, H. Boumgärtel, J. Electrochem. Soc. 137 (1990) 3626.
[18] O.J. Glembocki, E.D. Palik, G.R. De Guel, D.L. Kendall, J. Electrochem. Soc. 138 (1991) 1055.
[19] R.W. Schutz, Corrosion: Materials, vol. 13B, ASM Handbook, ASM International, Material Park, 2005.
[20] X.G. Zhang, Electrochemistry of Silicon and its Oxide, Kluwer Academic Publishers, New York, 2004.
[21] T. Tsuda, R. Hagiwara, J. Fluorine Chem. 129 (2008) 4.
[22] T. Tsuda, T. Nohira, K. Amezawa, K. Hachiya, R. Hagiwara, O. Raz, Y. Ein-Eli, Electrochim. Acta 53 (2008) 3650.
[23] J. Read, K. Mutolo, M. Ervin, W. Behl, J. Wolfenstine, A. Driedger, D. Foster, J. Electrochem. Soc. 150 (2003) A1351.
[24] J. Read, J. Electrochem. Soc. 149 (2002) A1190.
[25] P. Czuprynski, O. Joubert, J. Vac. Sci. Technol. B 16 (1998) 1051.
[26] J.T. Beak, H.H. Park, K.I. Cho, H.J. Yoo, S.W. Kang, B.T. Ahn, J. Appl. Phys. 78 (1995) 7074.
[27] S.W. Eom, C.W. Lee, M.S. Yun, Y.K. Sun, Electrochim. Acta 52 (2006) 1592.
[28] C. Tran, X.Q. Yang, D. Qu, J. Power Sources 195 (2010) 2057.
[29] S.S. Zhang, D. Foster, J. Read, J. Power Sources 195 (2010) 1235.
[30] O. Raz, Z. Shmueli, R. Hagiwara, Y. Ein-Eli, J. Electrochem. Soc. 157 (2010) H281.